Low-Temperature Synthesis of Tunable Mesoporous Crystalline Transition Metal Oxides and Applications as Au Catalyst Supports

Donghai Wang,[†] Zhen Ma,[§] Sheng Dai,[§] Jun Liu,[†,]* Zimin Nie,[†] Mark H. Engelhard,[‡] Qisheng Huo,[†] Chongmin Wang,[‡] and Rong Kou[†]

Chemical and Materials Science Division, Institute for Interfacial Catalysis, and Environmental Molecular Science Laboratory Pacific Northwest National Laboratory Richland, Washington, 99352, Chemical Sciences Division, Oak Ridge National Laboratory, Oak Ridge, Tennessee, 37831

Mesoporous transition metal oxides are of great potential as catalyst supports, shape-selective catalysts, photocatalysts, and sensor materials. Previously stable crystalline mesoporous oxides were mostly obtained by thermally induced crystallization or by segregating the nanocrystals with an amorphous phase. Here we report a novel direct approach to crystalline mesoporous frameworks via the spontaneous growth and assembly of transition metal oxide nanocrystals (i.e., rutile TiO_2, fluorite CeO_2, cassiterite SnO_2, and anatase $Sn_xTi_{1-x}O_2$) by oxidative hydrolysis and condensation in the presence of anionic surfactants. The influences of synthesis time, surfactants with different chain lengths, concentrations of the oxidant (i.e., hydrogen peroxide), and synthesis temperatures on the composition and morphologies of the resulting materials were investigated by X-ray diffraction, N_2-sorption, transmission electron microscopy, selected area electron diffraction, scanning electron microscopy, and X-ray photoelectron spectroscopy. A mechanism for the templated synthesis of crystalline mesoporous metal oxides was tentatively proposed. To demonstrate the catalytic applications of these materials, gold nanoparticles were loaded on mesoporous rutile TiO_2 and fluorite CeO_2 supports, and their catalytic performance in CO oxidation and water-gas shift was surveyed. Au nanoparticles supported on the mesoporous crystalline metal oxides exhibit higher reactivity and excellent on-stream stability toward CO oxidation and water-gas shift reaction compared with Au nanoparticles supported on commercial TiO_2 and CeO_2.

1. Introduction

Since the discovery of mesoporous silica (e.g., MCM-41 and SBA-15) in the 1990s,[1,2] large varieties of mesoporous metal oxides (e.g., titania, zirconia, alumina, niobia, and tantala) have been synthesized via various approaches for potential applications in catalysis and energy converstion.[3–6] A conventional soft-templating approach involves one-pot synthesis of metal oxides in the presence of surfactants as structure-directing agents.[7–9] However, the resulting metal oxides usually exhibit poor crystallinity (i.e., amorphorous or semicrystalline frameworks) and low thermal stability, which limit their applications as catalyst supports, photocatalysts, and electrode materials. On the other hand, a hard-templating approach relies on the replication of presynthesized removable templates (e.g., mesoporous silica or carbon,[10,11] and polymer or silica lattices[12]) and the subsequent removal of the templates via etching or calcination. Although this approach may lead to crystalline mesoporous metal oxides under certain conditions, it suffers from multiple and tedious steps as well as low yields to the desired products.

Considering that crystalline mesoporous metal oxides may exhibit enhanced thermal and mechanical stability as well as superior electric and optical properties, attempts have been made to synthesize these materials.[13–16] One viable approach to obtain crystalline mesoporous metal oxides is via the high-temperature crystallization of amorphous metal oxides in the presence of amorphous glass phases (e.g., silica,[17] phosphorus oxide,[15] and carbon[18]). The filled amorphous glass phases may mitigate the growth of nanocrystals into large grains during the high-temperature treatment, thus reinforcing the mesoporous frameworks. Alternatively, crystalline mesoporous metal oxides can be directly synthesized through low-temperature crystallization[19] or self-assembly of functionalized nanoparticles.[20] Recently, we have discovered that crystalline mesoporous titania prepared by low-temperature crystallization within functional surfactant matrix shows high Li-ion insertion capability and good reversibility as anodes in Li-ion battery.[21]

In this paper we further explore the low-temperature solution growth and crystallization routes for several transition metal oxides and report a novel direct approach to crystalline mesoporous metal oxides (i.e., TiO_2, CeO_2, SnO_2, and $Sn_xTi_{1-x}O_2$) composed of nanosized metal oxide building blocks (Scheme 1). We select anionic sulfate and sulfonate surfactants that can strongly interact with metal cations (e.g., Ce^{3+}, Sn^{2+}, and Ti^{3+}) to form mesostructured metal cation–surfactant composites. These metal cations are cross-linked to form M–O–M bonds, via a mild oxidative hydrolysis reaction controlled by an oxidant (i.e., H_2O_2), and transformed into nanosized TiO_2, CeO_2, SnO_2, and $Sn_xTi_{1-x}O_2$ building blocks in the presence of anionic sulfate surfactants.[22] The nanocrystals further form three-dimensional networks during calcination to remove surfactants. In this approach, anionic surfactants that strongly interact with metal cations or metal oxide species serve

* To whom correspondence should be addressed. Fax: (509) 375-3864. E-mail: jun.liu@pnl.gov.
† Chemical and Materials Science Division and Institute for Interfacial Catalysis, Pacific Northwest National Laboratory.
‡ Environmental Molecular Science Laboratory, Pacific Northwest National Laboratory.
§ Oak Ridge National Laboratory.

SCHEME 1: A Schematic Illustration of the Formation of Mesoporous Crystalline Metal Oxides Showing Nucleation and Crystallization of Metal Oxide Nanocrystals within Surfactant Matrix
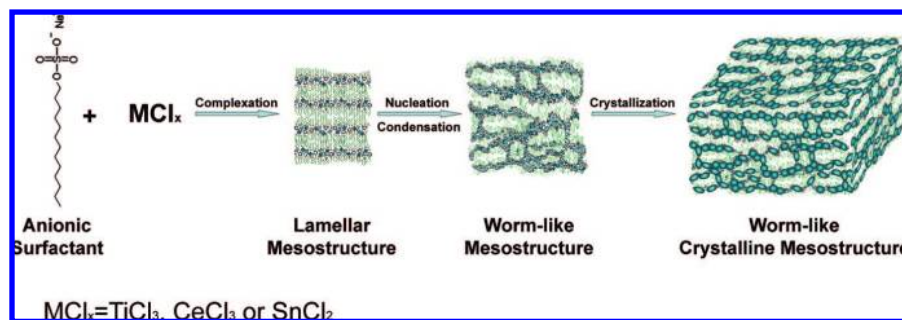
as pore-directing agents, instead of using cationic surfactants,[19] nonionic surfactants,[23,24] and block copolymers[25] previously reported. The slow oxidative hydrolysis and condensation of metal oxide precursors are a promising addition to low-temperature sol−gel crystallization processes[19] in the synthesis of mesoporous materials.

On the basis of this synthetic protocol, we systematically investigate the influences of synthesis time, different anionic surfactants, concentrations of the oxidant, synthesis temperatures, and metal oxide precursors on the composition and morphologies of the resulting materials by X-ray diffraction (XRD), N_2-sorption, transmission electron microscopy (TEM), selected area electron diffraction (SAED), scanning electron microscopy (SEM), and X-ray photoelectron spectroscopy (XPS). To demonstrate the applications, we load gold nanoparticles onto crystalline mesoporous TiO_2 and CeO_2, and investigate their catalytic activity and stability in CO oxidation and water-gas shift. Crystalline mesoporous metal oxides-supported gold nanoparticles exhibit high activity and enhanced thermal stability in these reactions. It is demonstrated in this study that our synthetic protocol is general, and the resulting materials are promising supports for gold nanocatalysts. In view of the wide applications of TiO_2, CeO_2, SnO_2, and $Sn_xTi_{1-x}O_2$ as catalyst components, photocatalysts, sensor materials, and battery electrodes, these new materials may open up a new avenue for further research and development.

2. Experimental Methods

2.1. Materials. Titanium trichloride ($TiCl_3$), cerium trichloride ($CeCl_3$), stannous chloride dihydrate ($SnCl_2 \cdot 2H_2O$), sodium dodecyl sulfate ($C_{12}H_{25}SO_4Na$), hexamethylenetetramine, 30 wt % hydrogen peroxide (H_2O_2), concentrated hydrochloric acid (HCl), and tetrachloroauric(III) acid trihydrate ($HAuCl_4 \cdot 3H_2O$) were purchased from Sigma-Aldrich. Sodium tetradecyl-sulfate ($C_{14}H_{29}SO_4Na$), sodium n-decyl-1-sulfonate ($C_{10}H_{21}SO_3Na$), and sodium 1-hexadecanesulfonate ($C_{16}H_{33}SO_3Na$) were purchased from TCI America. A commercial TiO_2 support (P25) with a surface area of 48 m^2/g was obtained from Degussa. A commercial CeO_2 support (REacton, purity: 99.9%) with a surface area of 2 m^2/g was obtained from Alfa Aesar.

2.2. Synthesis and Characterization of MCTs. In a typical synthesis of MCT-Ti, 7.33 mL of 20 mg/ml $C_{10}H_{21}SO_3Na$ solution (0.6 mmol), 1.2 mL of 0.5 M $C_{12}H_{25}SO_4Na$ solution (0.6 mmol), or 3.94 mL of 20 mg/ml $C_{16}H_{33}SO_3Na$ (0.6 mmol) in 2.53 M HCl solution was added into 10 mL of 0.12 M $TiCl_3$ solution (1.2 mmol) under vigorous stirring. Then, 0.8 mL of 1.0 wt % H_2O_2 solution (0.24 mmol) was added dropwise under vigorous stirring, and deionized water was added under vigorous stirring till a total volume of 55 mL was reached.

In a typical synthesis of MCT-Ce, 2.4 mL of 0.5 M $C_{12}H_{25}SO_4Na$ solution (1.2 mmol), 9.5 mL of 40 mg/ml $C_{14}H_{29}SO_4Na$ solution (1.2 mmol), or 19.7 mL of 20 mg/ml $C_{16}H_{33}SO_3Na$ solution (1.2 mmol) was added into 10 mL of 0.12 M $CeCl_3$ solution (1.2 mmol) under vigorous stirring followed by the addition of 19.2 mL of 1.0 M hexamethylenetetramine and 0.9 mL of 1.0 wt % H_2O_2 solution (0.26 mmol) under vigorous stirring. Then deionized water was added until a total volume of 55 mL was reached.

In a typical synthesis of MCT-Sn, 0.2708 g of $SnCl_2 \cdot 2H_2O$ solution (1.2 mmol) was dissolved in 1 mL concentrated HCl, followed by the addition of 9 mL of deionized water. A 7.93 mL portion of 20 mg/ml $C_{10}H_{21}SO_3Na$ solution (0.6 mmol), 8.15 mL of 20 mg/ml $C_{12}H_{25}SO_3Na$ solution (0.6 mmol), or 4 mL of 20 mg/ml $C_{16}H_{33}SO_3Na$ solution (0.25 mmol) was added under vigorous stirring. Then, 4.8 mL of 1.0 M hexamethylenetetramine was added to the mixture, followed by the addition of 4.0 mL of 1.0 wt % H_2O_2 solution (1.15 mmol). Finally, deionized water was added until a total volume of 55 mL was reached.

In a typical synthesis of MCT-Ti/Sn, 0.027 g of $SnCl_2 \cdot 2H_2O$ (0.12 mmol) was dissolved in 0.1 mL concentrated HCl followed by the addition of 5 mL of 0.24 M $TiCl_3$ (1.2 mmol). A 8.72 mL portion of 20 mg/ml $C_{10}H_{21}SO_3Na$ solution (0.66 mmol), 8.96 mL of 20 mg/ml $C_{12}H_{25}SO_3Na$ solution (0.66 mmol), or 4.4 mL of 20 mg/ml $C_{16}H_{33}SO_3Na$ solution (0.275 mmol) was added under vigorous stirring. Then, 0.5 mL of 1.0 M hexamethylenetetramine was added to the mixture, followed by the addition of 0.9 mL of 1.0 wt % H_2O_2 solution (0.26 mmol). Finally, deionized water was added until a total volume of 55 mL was reached.

All of these resulting mixtures were further stirred in a polypropylene flask at 60 °C for MCT-Ti or at 65 °C for MCT-Ce, MCT-Sn, and MCT-Ti/Sn for 15 h. The precipitates were separated by centrifuge followed by washing with deionized water and ethanol, and the product was then dried in a vacuum oven at 60 °C overnight and subsequently calcined in static air at a temperature specified in Table 1 for 2 h.

2.3. Synthesis of Supported Gold Catalysts. As-synthesized MCT-Ti-12 prepared using $C_{12}H_{25}SO_4Na$ as the template was calcined at 400 °C to remove the surfactant, washed several times with deionized water at 80 °C, and dried at 85 °C overnight. Gold was loaded onto the support (denoted as MCT-Ti in Section 3.4) via a deposition-precipitation method.[26−30] First, 13 mL of $HAuCl_4$ solution containing 0.078 g of $HAuCl_4 \cdot 3H_2O$ was sampled into a beaker, and the pH value of the mixture was adjusted to 10.0 by 1.0 M KOH with vigorous stirring. The resulting solution was heated at 80 °C, 0.26 g support was added, and the slurry was magnetically stirred for

Tunable Mesoporous Crystalline Transition Metal Oxides

J. Phys. Chem. C, Vol. 112, No. 35, 2008 **13501**

TABLE 1: Experimental Parameters and Physical Properties of Crystalline Mesoporous Metal Oxides

	sample ID	surfactant template	calcination temperature (°C)	crystalline phase	d-spacing[a] (nm)	surface area (m²/g)	average pore size (nm)	pore volume (cm³/g)
TiO_2	MCT-Ti-10	$C_{10}H_{21}SO_3Na$	400	rutile (5% anatase)	7.06	266	2.2	0.26
	MCT-Ti-12	$C_{12}H_{25}SO_4Na$	400		7.42	300	3.1	0.27
	MCT-Ti-16	$C_{16}H_{33}SO_3Na$	450		8.10	245	3.8	0.32
CeO_2	MCT-Ce-12	$C_{12}H_{25}SO_4Na$	400	fluorite	4.88	199	2.1	0.13
	MCT-Ce-14	$C_{14}H_{29}SO_4Na$	400		5.20	210	2.3	0.16
	MCT-Ce-16	$C_{16}H_{33}SO_3Na$	450		6.46	146	2.8	0.22
SnO_2	MCT-Sn-10	$C_{10}H_{21}SO_3Na$	400	cassiterite	5.86	155	2.3	0.21
	MCT-Sn-12	$C_{12}H_{25}SO_3Na$	425		6.24	225	3.0	0.18
	MCT-Sn-16	$C_{16}H_{33}SO_3Na$	450		6.86	173	3.4	0.20
$Sn_xTi_{1-x}O_2$	MCT-Ti/Sn-10	$C_{10}H_{21}SO_3Na$	400	anatase	5.62	310	2.3	0.30
	MCT-Ti/Sn-12	$C_{12}H_{25}SO_3Na$	400		5.77	246	2.8	0.27
	MCT-Ti/Sn-16	$C_{16}H_{33}SO_3Na$	450		5.91	271	3.8	0.37

[a] d-spacing value of the first reflection peak in MCTs.

2 h. During the course of deposition−precipitation, droplets of 1.0 M KOH were added to keep the pH value around 9.0. The precipitates were separated by centrifuge, washed four times with deionized water, and dried at 40 °C for 2 days. For comparison, Au/P25 catalyst was prepared using a commercial TiO_2 support (Degussa P25), as reported in previous publications.[31,32]

Gold was also loaded onto calcined MCT-Ce-12 support (denoted as MCT-Ce in Section 3.4) synthesized using $C_{12}H_{25}SO_4Na$ as the template. The pH value of the solution during the course of deposition−precipitation was again readjusted to 9.0 using 1.0 M KOH, in order to offset the negative effect caused by the leaching of residual acids from MCT-Ce surfaces. The precipitates were separated by centrifuge, washed four times with deionized water, and dried at 40 °C for 2 days. For comparison, Au/commercial CeO_2 catalyst was prepared in a similar way except that the pH value was not readjusted because there is no residual acid in commercial CeO_2.

2.4. Material Characterization. XRD patterns were recorded on a Philips Xpert X-ray diffractometer using Cu Kα radiation at λ = 1.54 Å. TEM images and SAED patterns were obtained on a JEOL JSM-2010 TEM microscope operated at 200 kV. SEM experiments were carried out using a Hitachi S5200 operated at 25.0 kV. N_2 adsorption−desorption data were collected using a Quantachrome autosorb automated gas sorption system.

XPS measurements were performed using a Physical Electronics Quantum 2000 Scanning ESCA Microprobe with a focused monochromatic Al Kα X-ray (1486.7 eV) source and a spherical section analyzer. High-energy-resolution photoemission spectra were collected using a pass energy of 46.95 eV. For the $Ag3d_{5/2}$ line, these conditions produced full width at half-maximum (fwhm) of better than 0.77 eV. The binding energy (BE) scale is calibrated using the $Cu2p_{3/2}$ feature at 932.62 ± 0.05 eV and Au4f at 83.96 ± 0.05 eV from known standards. Low-energy electrons at ∼1 eV, 20 μA, and low-energy Ar^+ ions were used to minimize the surface charging.

2.5. Catalytic Reaction. Catalytic CO oxidation and water-gas shift were tested in a plug-flow microreactor (Altamira AMI-200). When measuring conversion curves, 50 mg of as-synthesized catalyst was loaded into a U-shaped quartz tube supported by quartz wool. The catalyst was pretreated online in 8% O_2 (balance He) at a specified temperature for 2.5 h and was then cooled. To run CO oxidation, the O_2−He stream was switched to 1% CO (balance air), and the reaction temperature was ramped either by immersing the U-shaped tube in acetone-liquid nitrogen and allowing the coolant in a Dewar bottle warm naturally or by using a furnace. For water-gas shift, the O_2−He
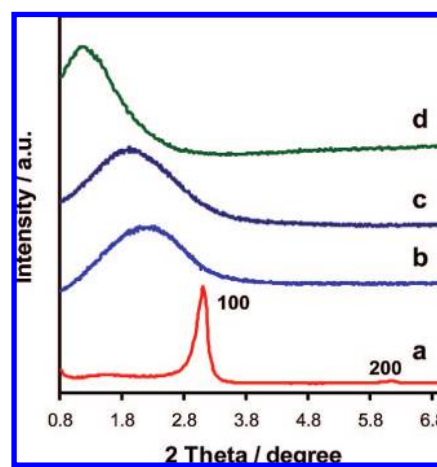

Figure 1. Low-angle XRD patterns of MCT-Ti-12 after immediate mixing of $TiCl_3$ and $C_{12}H_{25}SO_4Na$ surfactant (a), as-synthesized MCT-Ti-12 after 3 h reaction (b), as-synthesized MCT-Ti-12 after 15 h reaction (c), and calcined MCT-Ti-12 (d).

stream was switched to He to flush the system. Thereafter, 1% CO (balance He) was bubbled through a stainless steel saturator filled with water at room temperature and was continuously passed through the catalyst bed. The reaction temperature was ramped using a furnace. The flow rate of reactant streams in both reactions was 37 cm³/min. A portion of the product stream was periodically extracted with an automatic sampling valve and analyzed by a dual-column GC with a thermal conductivity detector. The CO conversion in both reactions was denoted as $X_{CO} = [CO_2]_{out}/([CO]_{out} + [CO_2]_{out})$. When measuring the catalyst stability as a function of reaction time, the identical pretreatment procedure was adopted, and the reaction conditions (e.g., catalyst load and flow rate) were generally adopted as described above unless otherwise specified in the text and figure captions.

3. Results and Discussion

3.1. Crystalline Mesoporous TiO_2. The structural evolution of MCT-Ti-12 at several stages of its synthesis was followed by XRD examination (Figure 1). The mixing of $TiCl_3$ and $C_{12}H_{25}SO_4Na$ leads to the instant formation of purple-yellowish precipitates. The XRD pattern shows a sharp diffraction peak at $2\theta = 3.0°$, together with a small peak at $2\theta = 6.1°$ (pattern a in Figure 1), indicative of a typical lamellar mesostructure with a (001) d-spacing of 2.88 nm. No crystalline structure is observed in the high-angle region (data not shown), meaning that the precipitates formed at this stage are still amorphous.
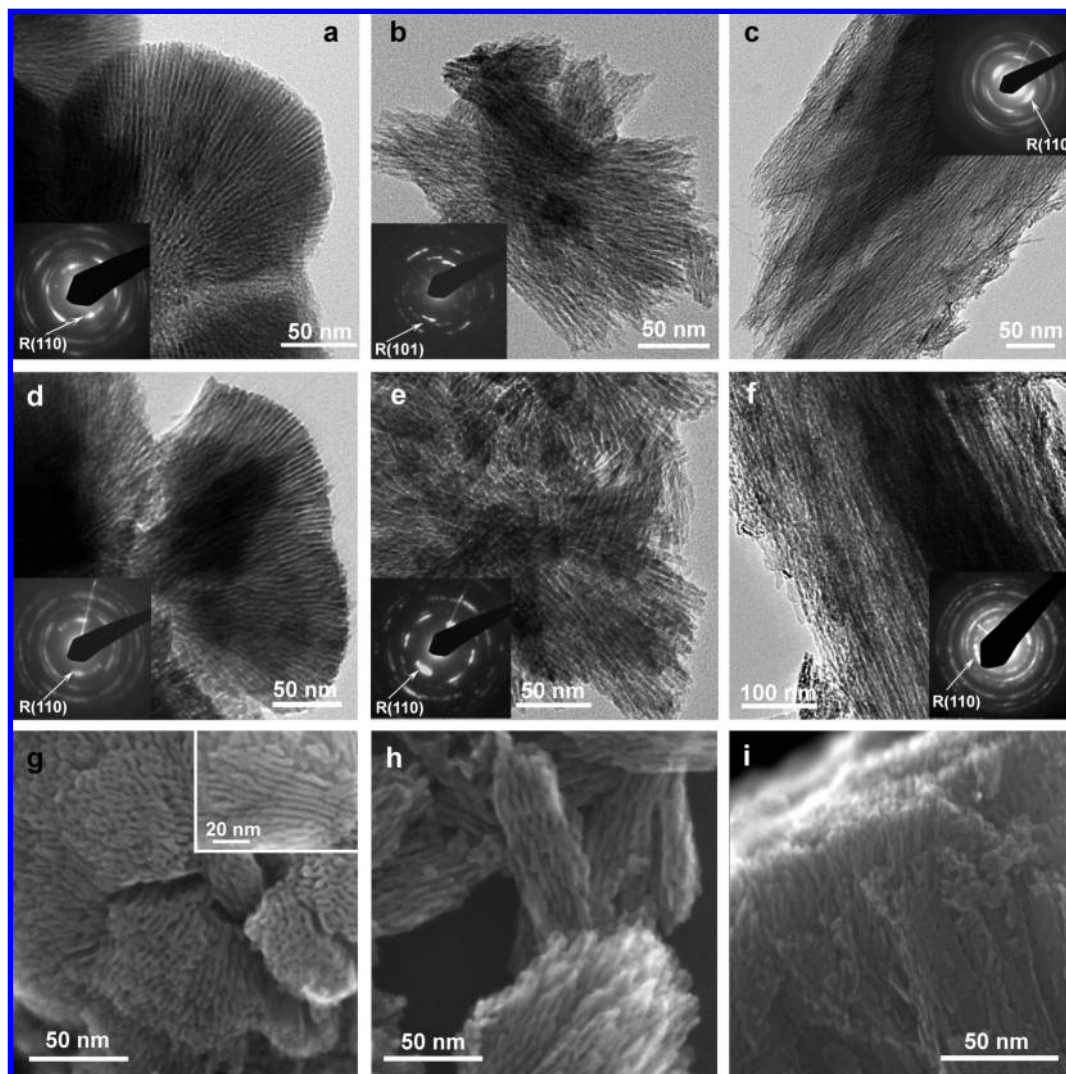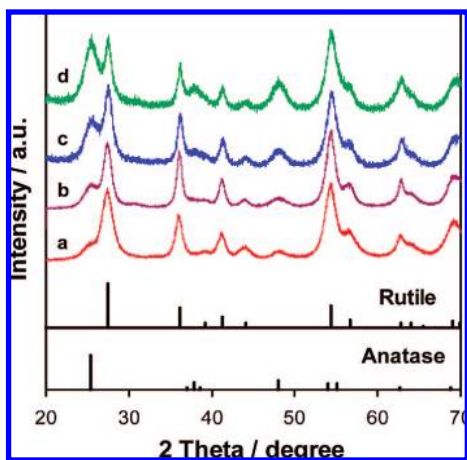
Figure 2. Typical TEM, high-resolution SEM images, and insets corresponding to SAED patterns of MCT-Ti. (a−c) TEM images of as-synthesized MCT-Ti-10 (a), MCT-Ti-12 (b), and MCT-Ti-16 (c). (d−f) TEM images of calcined MCT-Ti-10 (d), MCT-Ti-12 (e), and MCT-Ti-16 (f). (g−i) High-resolution SEM images of calcined MCT-Ti-10 (g), MCT-Ti-12 (h), and MCT-Ti-16 (i). The inset in panel g shows a side view of the stripe-patterned mesostructure composed of rod-like nanocrystals.

When the precipitates are aged in the solution at 60 °C for 3 h, the diffractions corresponding to the lamellar structure disappear, a broad low-angle peak appears at $2\theta = 2.2°$ (pattern b in Figure 1), and the diffraction peaks ascribed to rutile phase appear at high angles (data not shown), proving the formation of crystalline mesoporous structures. After being aged in the solution for 15 h, the precipitates exhibit a low-angle diffraction pattern similar to that of the precipitates collected after being aged for 3 h (pattern c in Figure 1). Finally, when the surfactant templates are removed via calcination in air, the low-angle diffraction peak shifts to $2\theta = 1.2°$ (pattern d in Figure 1), showing that the mesostructure has a thicker and denser framework. Overall, crystalline mesoporous structure of MCT-Ti-12 can be formed under mild synthesis conditions, and the mesostructure starting from lamellar mesophase still retains after removing the template.

To see whether the templated approach is general and to establish the structure−surfactant correlations, different anionic surfactants ($C_{10}H_{21}SO_3Na$, $C_{12}H_{25}SO_4Na$, and $C_{16}H_{33}SO_3Na$) were used to template the synthesis of MCT-Ti-10, MCT-Ti-12, and MCT-Ti-16, respectively, and the calcined samples were characterized by XRD and N_2 sorption. Their d-spacings, surface areas, average pore sizes, and pore volumes are summarized in

Table 1. Both the d-spacings and the average pore sizes of the calcined MCT-Ti samples increase along with the chain lengths of these surfactants, demonstrating that the pore sizes of these samples are tunable and that the surfactants may play an important role in this. It is also noteworthy that the surface areas of MCT-Ti-10, MCT-Ti-12, and MCT-Ti-16 samples are 266, 300, and 275 m^2/g, respectively, much higher than those of rutile TiO_2 prepared by high-temperature phase transformation.[33]

To get direct information on morphologies, a series of as-synthesized MCT-Ti samples were characterized by TEM (Figures 2a−c). In general, these samples all show "parallel" aggregation of rod-like features with periodic spacing. Specifically, the rod-like spaced features in MCT-Ti-10 are organized in semisphere grains and orient from the central region toward the edges (Figure 2a); MCT-Ti-12 consists of parallel rod-like TiO_2 strips interspaced by anionic surfactant domains (Figure 2b); and MCT-Ti-16 with larger grains shows similar parallel stripes as MCT-Ti-12. Interestingly, SAED patterns on striped grains of these samples reveal only rutile phase (insets in Figures 2a−c), rather than anatase phase obtained in the presence of sulfate ions on planar substrate reported previously.[34] The SAED patterns also show a pair of strong (110) (inset in Figures 2a

Tunable Mesoporous Crystalline Transition Metal Oxides

J. Phys. Chem. C, Vol. 112, No. 35, 2008 **13503**

Figure 3. Powder XRD patterns of calcined MCT-Ti-12 samples with increasing amount of H_2O_2 added in the reaction solution. (a) The regular amount of H_2O_2; (b) 125% of the regular amount of H_2O_2; (c) 137.5% of the regular amount of H_2O_2; (d) 150% of the regular amount of H_2O_2. Standard XRD peaks of rutile (JCPDS No. 21−1276) and anatase (JCPDS No. 21−1272) are shown as vertical bars.

and c) or (101) (inset in Figure 2b) reflections, indicating that the (110) or (101) planes of the rutile nanocrystals are well-aligned.

To know whether the above-mentioned morphologies still remain after the removal of the anionic templates, calcined MCT-Ti-10, MCT-Ti-12, and MCT-Ti-16 samples were further studied by TEM (Figures 2d−f) and high-resolution SEM (Figures 2g−i). As shown in Figures 2d−f, the overall mesostructures of these samples (i.e., rod-like rutile nanocrystals interspaced with straight mesopores) are well preserved. Pairs of strong (110) reflections spots in SAED patterns prove the presence of oriented rutile nanocrystals. High-resolution SEM data in Figures 2g−i further confirm the interspaced parallel organization of rod-like nanocrystals and mesopores in calcined MCT-Ti samples. Figure 2g shows mesopores as well as cross-linked feature of the rod-like nanocrystals from the top view of MCT-Ti-10, whereas radial organization of interspaced rod-like nanocrystals are clearly revealed in the inset of Figure 2g. Some nanocrystals are fused together, implying that the mesopores between nanorods are either cylindrical channels or slits. MCT-Ti-12 shows parallel assembly of mesopores and nanocrystals into rod-like grains, and the surface of the aggregates seems to be rough due to the extended long rods (Figure 2h). Similarly, MCT-Ti-16 exhibits parallel aggregated structures of rod-like nanocrystals interspaced by mesopores (Figure 2i). These TEM and SEM data again prove that MCT-Ti materials possess crystalline mesoporous structures.

The effect of the oxidant (i.e., H_2O_2) on the formation of rutile phase in MCT-Ti-12 was studied. It should be mentioned that the addition of H_2O_2 into the synthesis mixture is necessary to obtain crystalline products via oxidative hydrolysis. This point will be further elaborated in Section 3.3. As shown by the XRD data in Figure 3, the amount of anatase phase in the calcined MCT-Ti-12 increases when the amount of H_2O_2 exceeds the optimum value (0.8 mL of 1.0 wt % H_2O_2 in the synthesis mixture). Figure 4 shows TEM image of calcined MCT-Ti-12 prepared using 150% of the regular amount of H_2O_2. Under such synthesis condition, a significant amount of spherical anatase nanoparticle aggregates are observed instead of mesostructures composed of rutile nanorods. These results lead to the conclusion that excess H_2O_2 may cause the fast oxidation of the precursor and precipitation of anatase nanoparticles; rutile

nanorods are only formed by the slow and controlled oxidation of $TiCl_3$ within the surfactant matrix.

Synthesis temperature is an important factor that determines the composition and morphologies of the resulting materials. Figure 5 shows TEM images of calcined MCT-Ti-12 prepared at different temperatures. When the temperature is raised to 90 °C, rutile nanorods become thicker and parallel aggregates are barely observed (Figure 5a). When the synthesis temperature is further raised to 110 °C, the resulting products are mainly spherical anatase crystals, although rutile nanorods are occasionally observed (Figure 5b). It is well-known that the aggregated phase of surfactants is only stable below certain temperatures.[35] The ability of the surfactant to aggregate may be weakened under a higher reaction temperature (90 °C), leading to the formation of more-dispersed rutile nanorods. At an even higher temperature (110 °C), few surfactant aggregates may be formed, and anatase nanoparticles may precipitate directly from the solution. These results further demonstrate that the effective self-assembly surfactant matrix under mild conditions plays an important role in yielding rutile phase.

3.2. Crystalline Mesoporous CeO_2, SnO_2, and $Sn_xTi_{1−x}O_2$. To see whether the new synthesis protocol can be extended to other materials, we attempted to prepare crystalline CeO_2 (MCT-Ce), SnO_2 (MCT-Sn), and $Sn_xTi_{1−x}O_2$ (MCT-Ti/Sn) using this protocol. Figure 6 clearly reveals worm-like mesoporous structures with interconnected nanocrystalline frameworks in calcined MCT-Ce-12, MCT-Sn-16, and MCT-Ti/Sn-16 prepared using $C_{12}H_{25}SO_4Na$, $C_{16}H_{33}SO_3Na$, and $C_{16}H_{33}SO_3Na$ as templates, respectively. The materials prepared using other anionic surfactants with different chain lengths have similar worm-like mesoporous structures (data not shown). SAED patterns confirm that the frameworks of the MCTs are composed of polycrystalline metal oxide nanocrystals (insets in Figures 6a−c). In addition, high-resolution TEM images in Figures 6d−f clearly reveal that the mesoporous frameworks are composed of faceted or networked nanocrystals. The spacings between the adjacent lattice planes marked in Figures 6d−f are measured as 3.1, 3.3, and 3.5 Å, corresponding well to the values corresponding to the (111) planes of fluorite CeO_2, (110) planes of cassiterite SnO_2, and (101) planes of anatase TiO_2, respectively. An additional high-resolution SEM image of MCT-Sn-16 shows rod-like nanocrystals in the mesoporous framework (Figure S1 in the Supporting Information). The rod-like nanocrystals in the mesoporous framework may result in enhanced (101) reflection peaks in the high-angle XRD pattern.

The mesostructures and crystallinity of MCT-Ce, MCT-Sn, and MCT-Ti/Sn samples were investigated by XRD (Figure 7). The low-angle diffraction peaks of the calcined samples shift to high *d*-spacing values when increasing the surfactant chain length from $C_{10}H_{21}$-, $C_{12}H_{25}$-, or $C_{14}H_{29}$- to $C_{16}H_{33}$-, indicating the formation of tunable mesostructures (Figure 7a). Moreover, crystalline metal oxides have already been formed in as-synthesized MCTs (Figure 7b), just as the case with as-synthesized MCT-Ti samples. The estimated grain sizes of the nanocrystals in as-synthesized MCT-Ce-12, MCT-Sn-16, and MCT-Ti/Sn-16 samples are estimated by applying the Scherrer equation as 2.8, 2.3, and 3.8 nm, respectively. Well-defined high-angle reflection peaks are observed in the calcined MCTs corresponding to fluorite CeO_2, cassiterite SnO_2, and anatase TiO_2 (Figure 7b). Their estimated corresponding grain sizes are 4.2, 3.4, and 4.9 nm, respectively, consistent with the TEM data shown in Figure 6.

The mesoporosity of calcined samples was studied by N_2 sorption measurement. Calcined MCT-Ce shows type-IV iso-
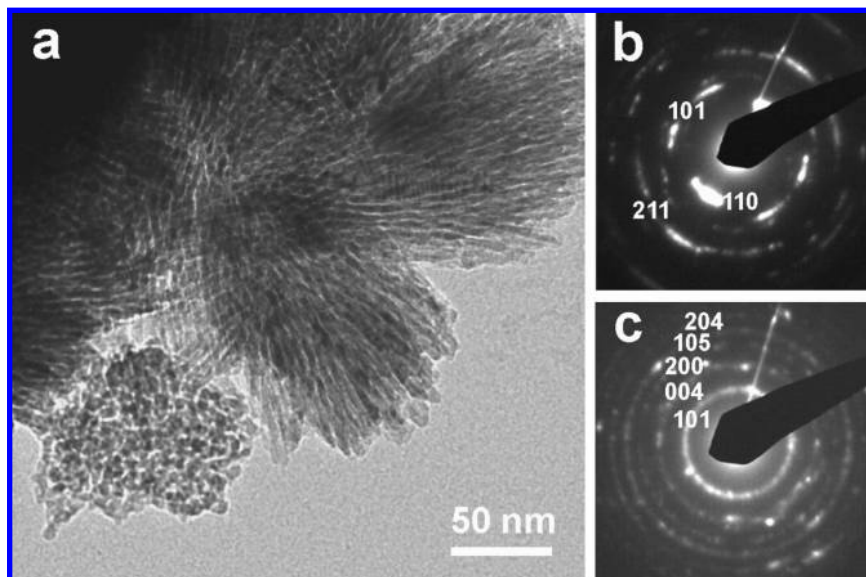
Figure 4. (a) TEM images of calcined MCT-Ti-12 synthesized with 150% of the regular amount of H_2O_2. It shows a mesoporous structure composed of rutile nanorods as well as a mesostructure composed of spherical anatase nanoparticles. (b and c) Selected area electron diffraction patterns of rutile nanorod mesostructure (b) and of anatase nanoparticle mesostructure (c).
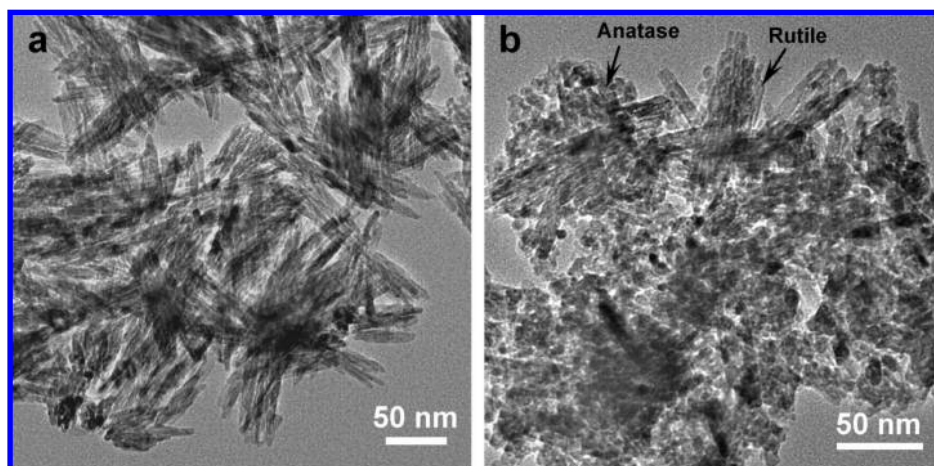

Figure 5. (a) TEM image of calcined MCT-Ti-12 synthesized at 90 °C showing the mesosturcture composed of thicker rutile nanorods.(b) TEM image of calcined MCT-Ti-12 synthesized at 110 °C showing aggregated rutile nanorods and spherical anatase nanoparticles.

therms (Figure 8a), and their average mesopore diameters increase from 2.5, 2.9, to 3.4 nm by changing chain length of the anionic surfactant from $C_{10}H_{21}$-, $C_{12}H_{25}$-, to $C_{16}H_{33}$-, respectively (Figure 8d). Similarly, calcined MCT-Sn (Figures 8b and e) and MCT-Ti/Sn (Figures 8c and f) also show type-IV isotherms with narrow distribution of mesopore diameters. The mesopore diameters of the MCT-Sn and MCT-Ti/Sn can also be systematically tuned by altering the chain lengths of the anionic surfactants (i.e., $C_{10}H_{21}$-, $C_{12}H_{25}$-, and $C_{16}H_{33}$-). The BET surface areas, average pore size, and pore volume calculated from nitrogen sorption are summarized in Table 1. It should again be emphasized that the surface areas of these crystalline materials are high (146−310 m²/g), confirming that the templated oxidative hydrolysis method is a successful approach to obtain crystalline mesoporous TiO_2, CeO_2, SnO_2, and $Sn_xTi_{1-x}O_2$.

3.3. Formation of Mesoporous Crystalline Metal Oxides. Different from the conventional synthesis of semicrystalline mesoporous metal oxides via templated sol−gel processing followed by high-temperature calcination, here we use the slow oxidative hydrolysis of transition metal cations (Ti^{3+}, Sn^{2+}, and Ce^{3+}) in aqueous solutions to form nanocrystalline metal oxides

directly. The nucleation and growth of nanocrystalline metal oxides is controlled via the hydrolysis and oxidation of metal cations by hydrogen peroxide and via the slow release of hydroxyl ions owing to thermal decomposition of hexamethylenetetramine in aqueous solutions. The chemical reaction is invoked as follows:

$$M^{3+/2+} + H_2O + H_2O_2 \rightarrow M(IV) \text{ oxy species} \rightarrow MO_2 \text{ (M} =$$

$$Ti^{3+}, Sn^{2+}, \text{ and } Ce^{3+})$$
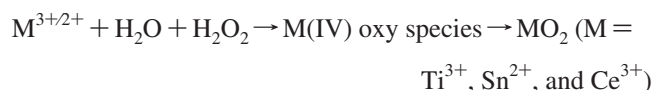
Hydrogen peroxide plays an important role in synthesizing crystalline metal oxides. In a control experiment without adding hydrogen peroxide, amorphous phase and only a small portion of crystallites in the products are observed by TEM. The obtained amorphous TiO_2 shows light blue color and CeO_2 shows light white color, in contrast to the white and yellowish colors exhibited by crystalline TiO_2 and CeO_2, respectively. This difference indicates that the amorphous product still contains incompletely oxidized Ti^{3+} or Ce^{3+}. Even after synthesis for a longer time (e.g., 30 h), crystalline metal oxides still can not be obtained except at elevated temperature (e.g., 140 °C or higher). However, at elevated temperatures, the domain sizes
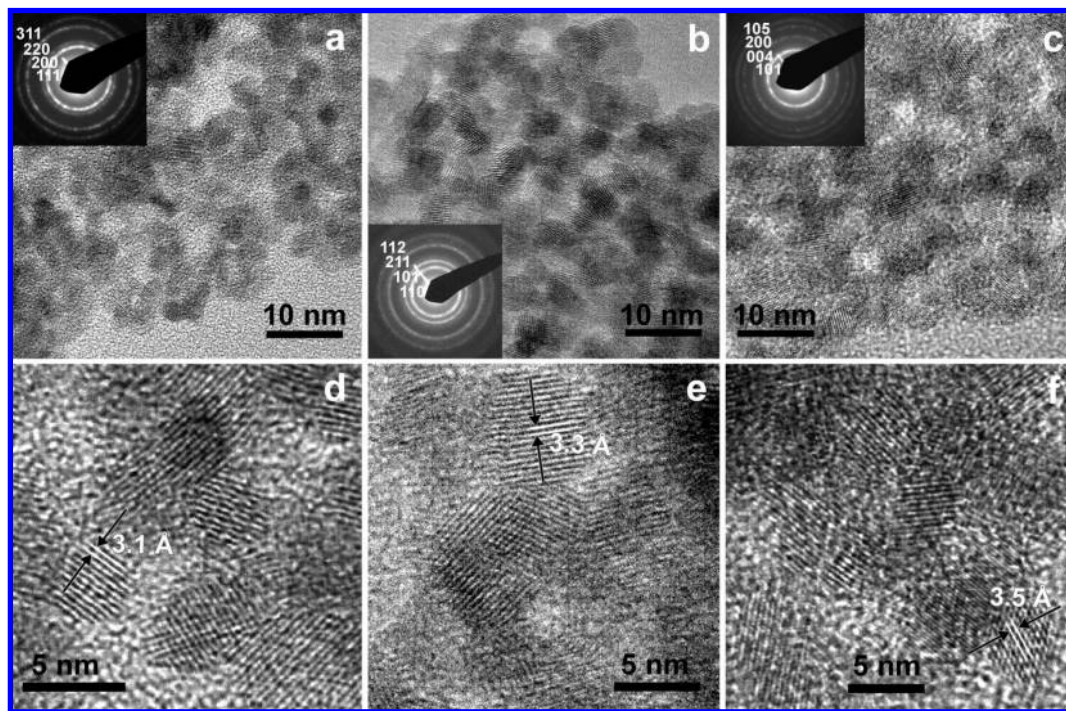
Figure 6. (a−c) TEM images of calcined MCT-Ce-12 (a), MCT-Sn-16 (b), and MCT-Ti/Sn-16 (c). The insets show SAED patterns corresponding to polycrystalline fluorite, cassiterite, and anatase structures. (d−f) High-resolution TEM images of CeO_2 (d), SnO_2 (e), and $Sn_xTi_{1-x}O_2$ (f) nanocrystalls in mesoporous framework of MCT-Ce-12, MCT-Sn-16, and MCT-Ti/Sn-16, respectively.
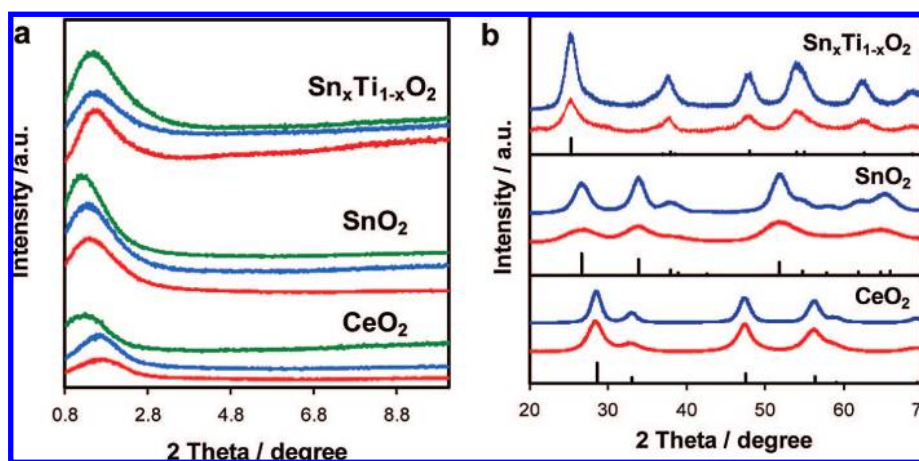
Figure 7. (a) Low-angle XRD patterns of calcined MCT-Ce, MCT-Sn, and MCT-Ti/Sn. The patterns of MCT-Ce prepared using C_{12}-, C_{14}-, and C_{16}- surfactants are displayed in red, blue, and green, respectively. The patterns of MCT-Sn and MCT-Ti/Sn prepared using C_{10}-, C_{12}-, and C_{16}- surfactants are displayed in red, blue and green, respectively. (b) High-angle XRD patterns of as-synthesized MCT-Ce-12, MCT-Sn-16, and MCT-Ti/Sn-16 (red bottom curves) compared with calcined samples (blue top curves). Standard diffraction peaks of fluorite CeO_2 (JCPDS No. 034−0394), cassiterite SnO_2 (JCPDS No. 000−0024), and anatase TiO_2 (JCPDS No. 21−1272) are shown as vertical bars.

of aggregated mesostructures decrease as shown in Figure 5, thus leading to large nanoparticles,[22] poor mesoporouss structures, and low surface area.

Because of the strong interaction between the sulfate group and the metal cations, the anionic surfactant and the metal cations complex with each other to form ordered mesostructures (i.e., lamellar mesostructures). Although anionic surfactant templated metal oxide mesostructures have been previously investigated,[49] the slow oxidative hydrolysis and condensation provide a low-temperature crystallization pathway to directly synthesize robust metal oxide nanocrystals in the as-synthesized mesostructured metal oxide/surfactant composites, rather than amorphous metal oxides.[36,21] On the basis of the above experimental investigation, we suggest that the formation of MCTs starts from lamellar mesostructured metal cation/surfac-

tant composites followed by nucleation and growth of metal oxide nanocrystals within anionic surfactant matrix, and eventually results in anionic surfactant interspaced worm-like mesostructured nanocrystal frameworks (Scheme 1).

3.4. Synthesis and Catalytic Performance of Au/MCTs. Catalysis by finely divided gold nanoparticles has attracted great attention recently.[26−30] The majority of gold catalysts reported in the literature are prepared by loading gold onto commercial nonporous supports, whereas the use of both porous supports (e.g., mesoporous materials)[37−41,34,42−46] and nanosized supports (e.g., nanoparticles, nanotubes, and nanorodes)[47−52] in this regard has received insufficient attention. It is of interest to explore the catalytic performance of gold on nanocrystalline porous supports because curvatured mesopores may provide additional interfacial sites and confinement environments, whereas gold
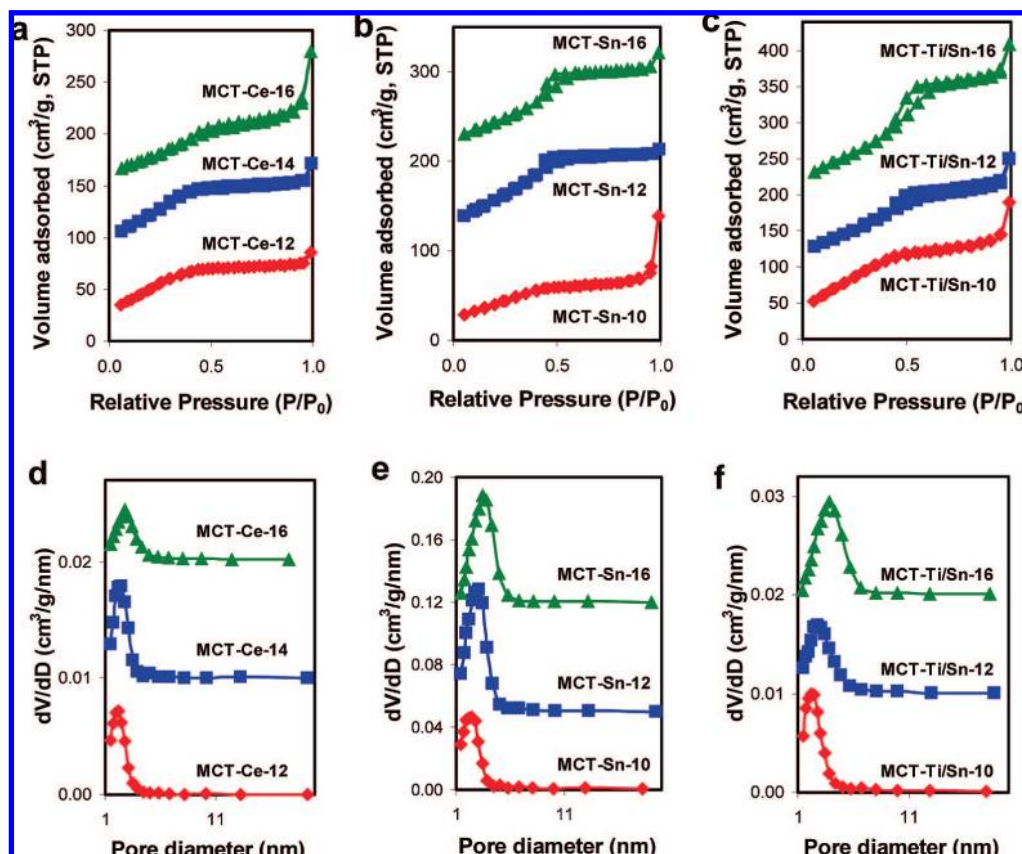
Figure 8. (a–c) N$_2$ sorption isotherms of calcined MCT-Ce (a), MCT-Sn (b), and MCT-Ti/Sn (c). The isotherms of MCT-Ce-14, MCT-Ce-16, MCT-Sn-12, MCT-Sn-16, MCT-Ti/Sn-12, and MCT-Ti/Sn-16 are offset vertically by 70, 140, 100, 200, 80, and 180 cm^3/g, respectively. (d–f) Pore size distribution of mesopore diameters for MCT-Ce (d), MCT-Sn (e), and MCT-Ti/Sn (f). The distribution was calculated via the Barrett–Joyner–Halenda (BJH) model using the adsorption branch. The distribution of MCT-Ce-14, MCT-Ce-16, MCT-Sn-12, MCT-Sn-16, MCT-Ti/Sn-12, and MCT- Ti/Sn-16 are offset vertically by 0.01, 0.02, 0.05, 0.12, 0.01, and 0.02 cm^3/g/nm, respectively.
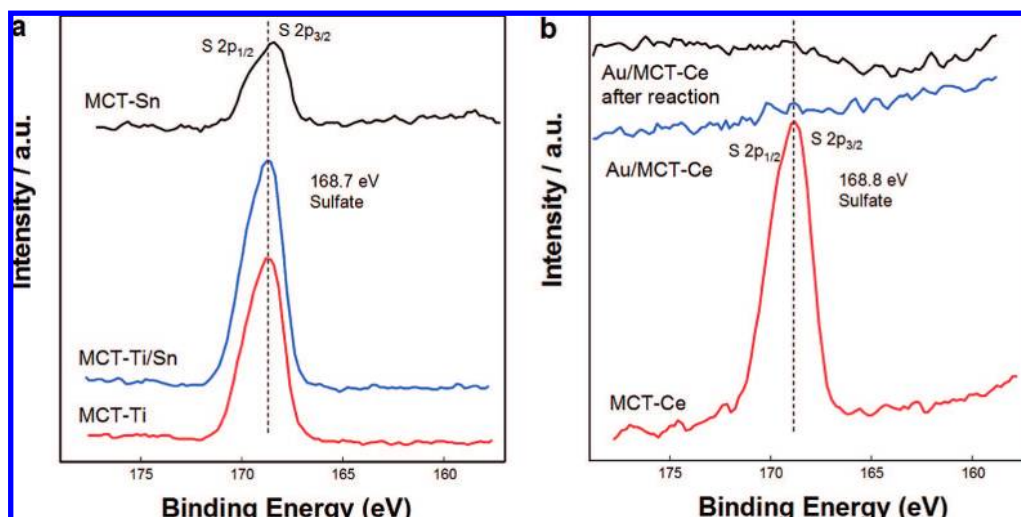

Figure 9. (a) High-energy-resolution XPS spectra of the S 2p region in calcined MCT-Ti-12, MCT-Sn-16, and MCT-Ti/Sn-16. (b) XPS spectra of the S 2p region in calcined MCT-Ce-12, as-synthesized Au/MCT-Ce-12, and Au/MCT-Ce-12 collected after 400 °C-pretretment and subsequent CO oxidation.

nanoparticles supported on metal oxide nanocrystals often exhibit superior catalytic performance than those supported on bulk supports.[47–49] To demonstrate the applications of crystalline mesoporous materials, here we supported gold nanoparticles onto rutile TiO$_2$ and fluorite CeO$_2$ and have tested their performance in CO oxidation and water-gas shift reaction.

One detail on the preparation of Au/MCTs catalysts is that the pH value during their synthesis was readjusted to 9.0.

As shown by the XPS data in Figure 9, the calcined MCTs still contain detectable sulfate species. These acidic species dissolve into the solution during deposition–precipitation, thus decreasing the pH value and lowering the activity of the resulting gold catalysts (see a control experiment in Figure S2 in the Supporting Information where the pH was not readjusted and the pH value dropped to 5.0, resulting in inferior activity in CO oxidation). Ma et al. previously
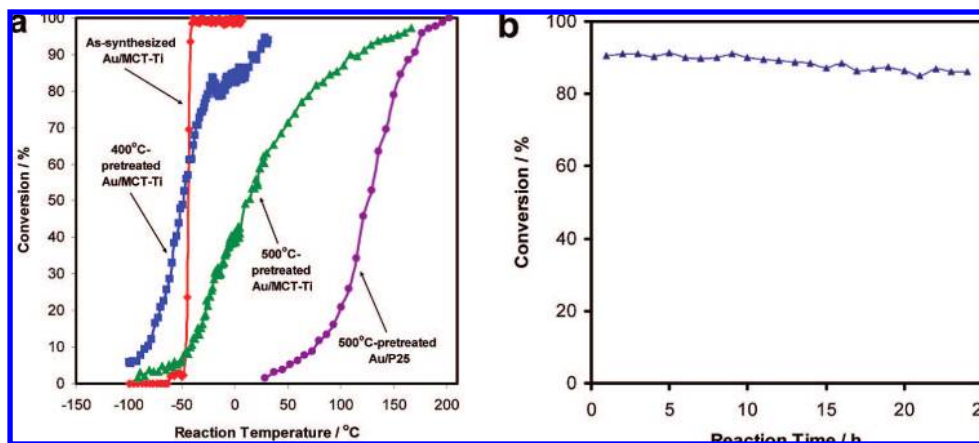
Figure 10. Catalytic performance of Au/MCT-Ti for low-temperature CO oxidation. (a) Light-off curves of as-synthesized Au/MCT-Ti, 400 °C-pretreated Au/MCT-Ti, 500 °C-pretreated Au/MCT-Ti, and 500 °C-pretreated Au/P25. (b) CO conversion at 24 on 400 °C-pretreated Au/MCT-Ti as a function of reaction time.
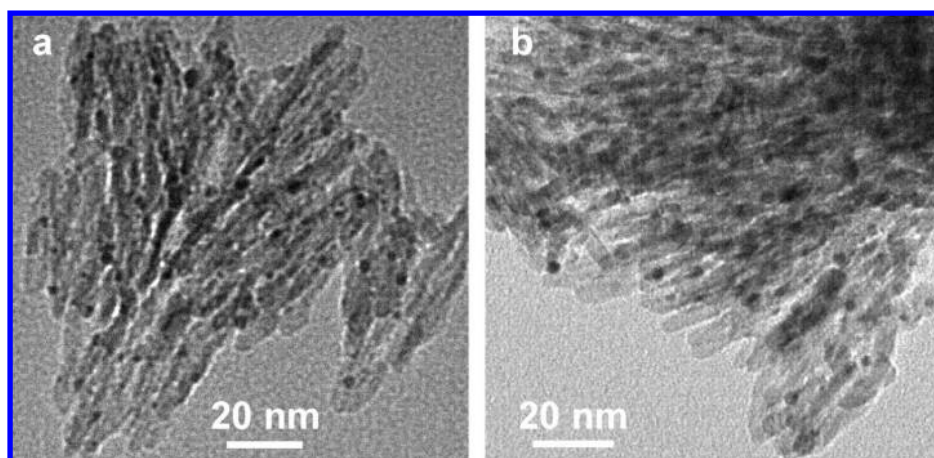
Figure 11. TEM images of as-synthesized Au/MCT-Ti collected after reactions testing (a) and of 400 °C-pretreated Au/MCT-Ti collected after reaction testing (b).

showed that the leaching of phosphate from PO_4^{3-}/TiO_2 may influence the performance of Au/PO_4^{3-}/TiO_2 catalysts, and this issue can be tackled by readjusting the pH value.[31] Therefore, here we readjusted the pH value to 9.0 during depositon−precipitation by adding droplets of KOH. As a result, the pH environment remains optimal for the synthesis of active gold catalysts,[53] and there is no detectable sulfate species on as-synthesized Au/MCTs (Figure 9b).

The catalytic performance of Au/MCT-Ti in CO oxidation is compared to that of Au/P25 (Figure 10a). As-synthesized Au/P25, without undergoing thermal pretreatment, is very active, achieving 50% CO conversion at −39 °C. The temperature required for 50% conversion is referred to as "T_{50}". However, after the as-synthesized Au/P25 is pretreated at 500 °C prior to the reaction testing, its T_{50} value increased to 126 °C, indicating a significant decrease in activity.[31,32] On the other hand, as-synthesized Au/MCT-Ti is very active, achieving T_{50} values at −44 °C. After pretreating this catalyst at 400 °C, its T_{50} value is −49 °C. Even after pretreating Au/MCT-Ti at 500 °C, the catalyst is still active (T_{50} = 13 °C) compared with 500 °C-pretreated Au/P25 (T_{50} = 126 °C). The specific rates of 500 °C-pretreated Au/MCT-Ti and Au/P25 are calculated as 0.163 and 0.006 mol·g_{Au}^{-1}·h^{-1} at 30 °C, considering their measured conversions (63 and 1.7%), gold loadings (7.0 and 5.6 wt%), gas concentration (1% CO), and flow rate (37 cm^3/min).

The stability of Au/MCT-Ti catalyst was also tested as a function of reaction time. The catalyst was pretreated at 400

°C prior to the reaction testing. As shown in Figure 10b, there is only minor deactivation on stream at the reaction temperature of 24 °C, consistent with the slowly decreasing trend obtained with mesoporous Au/TiO_2 previously reported.[44]

The activity difference between Au/MCT-Ti and Au/P25 samples may be due to the size of gold nanoparticles; whereas gold nanoparticles on a commercial Degussa P25 support sinter after 500 °C-pretretment (5−30 nm),[31,32] those on MCT-Ti support are still small even after high-temperature pretreatment (Figure 11). This antisintering ability of our catalysts is an important feature because the sintering of gold nanoparticles is a practical issue to be tackled for industrial applications.[54] The curvatured mesoporous rutile supports may play an important role in stabilizing gold nanoparticles. Alternatively, the anchoring of sulfate species during the synthesis of mesoporous TiO_2 and the leaching of sulfate species during the deposition−precipitation of gold may create surface defects for stabilizing gold nanoparticles.[55]

The catalytic performance of Au/MCT-Ce in CO oxidation is compared to that of Au/commercial CeO_2. Both 200 and 500 °C-pretreated Au/MCT-Ce catalysts are very active in CO oxidation, achieving T_{50} values at around −18 and −25 °C, respectively (Figure 12a). For comparison, the T_{50} values of 200 and 500 °C-pretreated Au/commercial CeO_2 in CO oxidation are 30 and 132 °C, respectively. In this case, the surface area of our MCT-Ce support is 199 m^2/g, whereas that of the commercial CeO_2 support is only 2 m^2/g. The 500 °C-pretreated

13508 *J. Phys. Chem. C, Vol. 112, No. 35, 2008*

Wang et al.
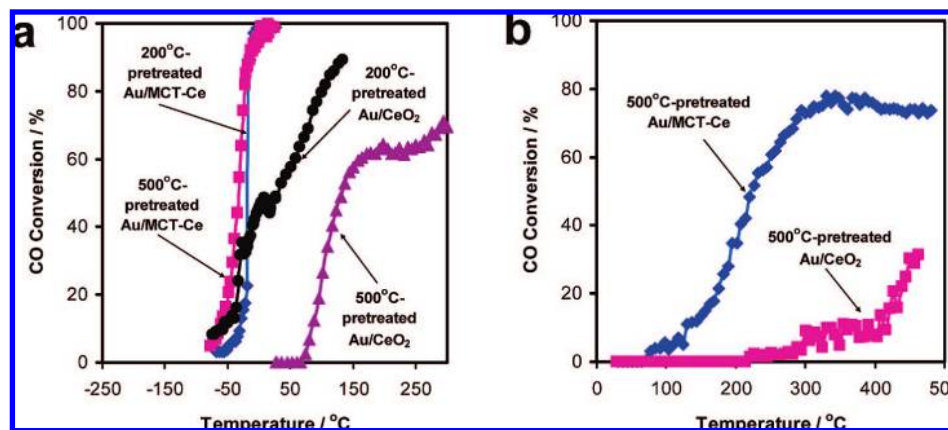
Figure 12. (a) Conversion curves of 200 °C-pretreated Au/MCT-Ce and Au/commercial CeO$_2$ as well as 500 °C-pretreated Au/MCT-Ce and Au/commercial CeO$_2$ in CO oxidation. (b) Conversion curves of 500 °C-pretreated Au/MCT-Ce and Au/commercial CeO$_2$ in water-gas shift reaction.

Au/MCT-Ce also has good stability on stream (Figure S3a in the Supporting Information). To measure the stability correctly, 45 mg catalyst was used instead of the regular load (50 mg), and the flow rate was increased to 50 mL/min compared to the regular flow rate (37 mL/min) in order to avoid observing 100% conversion all the time.

The performance of Au/MCT-Ce in water-gas shift reaction is also compared to that of Au/commercial CeO$_2$. The 500 °C-pretreated Au/MCT-Ce catalyst is much more active than Au/commercial CeO$_2$ in water-gas shift, obtaining 73% CO conversion at 296 °C (Figure 12b). The CO conversion on the catalyst in water-gas shift reaction remains stable on stream over 70 h (Figure S3b in Supporting Information). On the other hand, 500 °C-pretreated Au/commercial CeO$_2$ only shows 2.3% conversion at 296 °C (Figure 12b). The high activity of Au/MCT-Ce is ascribed to the high surface area of the support as well as the optimized interaction between gold nanoparticles and nanosized CeO$_2$ building blocks. Corma and co-workers previously reported that gold nanoparticles on nanosized CeO$_2$ exhibits much higher activity in CO oxidation than Au/commercial CeO$_2$.[48] Overall, our catalysis results indicate that crystalline mesoporous transition metal oxides are indeed useful as catalyst supports.

4. Conclusion

We have developed a novel, generalized low-temperature approach for the direct synthesis of crystalline mesoporous metal oxides (e.g., TiO$_2$, CeO$_2$, SnO$_2$, and Sn$_x$Ti$_{1-x}$O$_2$). Metal oxide nanocrystals are grown within organized anionic surfactant/metal cation mesostructures via slow oxidative hydrolysis and condensation, and the mesostructures still maintain after the removal of anionic surfactant templates via calcination. The mesopore diameters increase consistently with the chain lengths of the anionic surfactants, showing the importance of templates in the formation of these mesostructures. The optimum synthesis temperature is 60−65 °C, whereas high synthesis temperatures (e.g., 110 °C) influence the organization of mesostructures. The concentration of the oxidant (i.e., H$_2$O$_2$) also needs to be controlled in order to get rutile phase. Gold nanoparticles supported mesoporous rutile TiO$_2$ and fluorite CeO$_2$ show high catalytic activity and sustained on-stream stability for low-temperature CO oxidation and water-gas shift reaction. We believe that these crystalline mesoporous metal oxides and other materials potentially synthesized via this approach may be useful as

robust and high-surface-area supports and photocatalysts for other catalytic reactions, where conventionally prepared mesoporous materials suffer from low crystallinity and stability.

Supporting Information Available: High resolution scanning electron microscopy image of MCT-Sn, light-off curves of as-synthesized Au/MCT-Ti prepared at different conditions, and reaction stability result of Au/MCT-Ce. This material is available free of charge via the Internet at http://pubs.acs.org.

References and Notes

(1) Kresge, C.; Leonowicz, M.; Roth, W.; Vartuli, C.; Beck, J. *Nature* **1992**, *359*, 710.

(2) Zhao, D.; Feng, J.; Huo, Q.; Melosh, N.; Frederickson, G. H.; Chmelka, B. F.; Stucky, G. D. *Science* **1998**, *279*, 548.

(3) Antonelli, D. M.; Ying, J. Y. *Angew. Chem.-Int. Ed. Engl.* **1995**, *34*, 2014.

(4) Ulagappan, N.; Rao, C. N. R. *Chem. Commun.* **1996**, *1685*.

(5) Severin, K. G.; Abdel-Fattah, T. M.; Pinnavaia, T. J. *Chem. Commun.* **1998**, *1471*.

(6) Lyons, D. M.; Ryan, K. M.; Morris, M. A. *J. Mater. Chem.* **2002**, *12*, 1207.

(7) Antonelli, D. M.; Ying, J. Y. *Angew. Chem.-Int. Ed. Engl.* **1996**, *35*, 426.

(8) Antonelli, D. M.; Ying, J. Y. *Chem. Mater.* **1996**, *8*, 874.

(9) Yang, P. D.; Zhao, D. Y.; Margolese, D. I.; Chmelka, B. F.; Stucky, G. D. *Chem. Mater.* **1999**, *11*, 2813.

(10) Katou, T.; Lee, B.; Lu, D. L.; Kondo, J. N.; Hara, M.; Domen, K. *Angew. Chem.-Int. Ed.* **2003**, *42*, 2382.

(11) Tian, B. Z.; Liu, X. Y.; Solovyov, L. A.; Liu, Z.; Yang, H. F.; Zhang, Z. D.; Xie, S. H.; Zhang, F. Q.; Tu, B.; Yu, C. Z.; Terasaki, O.; Zhao, D. Y. *J. Am. Chem. Soc.* **2004**, *126*, 865.

(12) Holland, B. T.; Blanford, C. F.; Do, T.; Stein, A. *Chem. Mater.* **1999**, *11*, 795.

(13) Qi, L. M.; Ma, J. M.; Cheng, H. M.; Zhao, Z. G. *Langmuir* **1998**, *14*, 2579.

(14) Crepaldi, E. L.; Soler-Illia, G.; Bouchara, A.; Grosso, D.; Durand, D.; Sanchez, C. *Angew. Chem.-Int. Ed.* **2003**, *42*, 347.

Tunable Mesoporous Crystalline Transition Metal Oxides

J. Phys. Chem. C, Vol. 112, No. 35, 2008 **13509**

(15) Li, D. L.; Zhou, H. S.; Honma, I. *Nat. Mater.* **2004**, *3*, 65.

(16) Kondo, J. N.; Domen, K. *Chem. Mater.* **2008**, *20*, 835.

(17) Dong, W. Y.; Sun, Y. J.; Lee, C. W.; Hua, W. M.; Lu, X. C.; Shi, Y. F.; Zhang, S. C.; Chen, J. M.; Zhao, D. Y. *J. Am. Chem. Soc.* **2007**, *129*, 13894.

(18) Lee, J.; Orilall, M. C.; Warren, S. C.; Kamperman, M.; Disalvo, F. J.; Wiesner, U. *Nat. Mater.* **2008**, *7*, 222.

(19) Shibata, H.; Ogura, T.; Mukai, T.; Ohkubo, T.; Sakai, H.; Abe, M. *J. Am. Chem. Soc.* **2005**, *127*, 16396.

(20) Corma, A.; Atienzar, P.; Garcia, H.; Chane-Ching, J. Y. *Nat. Mater.* **2004**, *3*, 394.

(21) Wang, D. H.; Choi, D.; Yang, G. Z.; Viswanathan, V. V.; Nie, Z.; Wang, C. M.; Song, Y. J.; Zhang, J. G.; Liu, J. *Chem. Mater.* **2008**, *20*, 3435.

(22) Wang, D. H.; Liu, J.; Huo, Q. S.; Nie, Z. M.; Lu, W. G.; Williford, R. E.; Jiang, Y. B. *J. Am. Chem. Soc.* **2006**, *128*, 13670.

(23) Thieme, M.; Schüth, F. *Microporous Mesoporous Mater.* **1999**, *27*, 193.

(24) Grosso, D.; Boissiere, C.; Smarsly, B.; Brezesinski, T.; Pinna, N.; Albouy, P. A.; Amenitsch, H.; Antonietti, M.; Sanchez, C. *Nat. Mater.* **2004**, *3*, 787.

(25) Yang, P. D.; Zhao, D. Y.; Margolese, D. I.; Chmelka, B. F.; Stucky, G. D. *Nature* **1998**, *396*, 152.

(26) Bond, G. C.; Thompson, D. T. *Catal. Rev.-Sci. Eng.* **1999**, *41*, 319.

(27) Haruta, M.; Date, M. *Appl. Catal., A* **2001**, *222*, 427.

(28) Choudhary, T. V.; Goodman, D. W. *Top. Catal.* **2002**, *21*, 25.

(29) Hashmi, A. S. K.; Hutchings, G. J. *Angew. Chem.-Int. Ed.* **2006**, *45*, 7896.

(30) Kung, M. C.; Davis, R. J.; Kung, H. H. *J. Phys. Chem. C* **2007**, *111*, 11767.

(31) Ma, Z.; Brown, S.; Overbury, S. H.; Dai, S. *Appl. Catal., A* **2007**, *327*, 226.

(32) Ma, Z.; Overbury, S. H.; Dai, S. *J. Mol. Catal. A* **2007**, *273*, 186.

(33) Samuel, V.; Muthukumar, P.; Gaikwad, S. P.; Dhage, S. R.; Ravi, V. *Mater. Lett.* **2004**, *58*, 2514.

(34) Chiang, C. W.; Wang, A. Q.; Mou, C. Y. *Catal. Today* **2006**, *117*, 220.

(35) Beck, J. S.; Vartuli, J. C.; Kennedy, G. J.; Kresge, C. T.; Roth, W. J.; Schramm, S. E. *Chem. Mater.* **1994**, *6*, 1816.

(36) Hosono, E.; Fujihara, S.; Kakiuchi, K.; Imai, H. *J. Am. Chem. Soc.* **2004**, *126*, 7790.

(37) Yang, C. M.; Kalwei, M.; Schüth, F.; Chao, K. J. *Appl. Catal., A* **2003**, *254*, 289.

(38) Liu, J. H.; Chi, Y. S.; Lin, H. P.; Mou, C. Y.; Wan, B. Z. *Catal. Today* **2004**, *93* (95), 141.

(39) Overbury, S. H.; Ortiz-Soto, L.; Zhu, H. G.; Lee, B.; Amiridis, M. D.; Dai, S. *Catal. Lett.* **2004**, *95*, 99.

(40) Chiang, C. W.; Wang, A. Q.; Wan, B. Z.; Mou, C. Y. *J. Phys. Chem. B* **2005**, *109*, 18042.

(41) Bore, M. T.; Mokhonoana, M. P.; Ward, T. L.; Coville, N. J.; Datye, A. K. *Microporous Mesoporous Mater.* **2006**, *95*, 118.

(42) Idakiev, V.; Tabakova, T.; Naydenov, A.; Yuan, Z. Y.; Su, B. L. *Appl. Catal., B* **2006**, *63*, 178.

(43) Zhu, H. G.; Liang, C. D.; Yan, W. F.; Overbury, S. H.; Dai, S. *J. Phys. Chem. B* **2006**, *110*, 10842.

(44) Denkwitz, Y.; Geserick, J.; Hormann, U.; Plzak, V.; Kaiser, U.; Husing, N.; Behm, R. J. *Catal. Lett.* **2007**, *119*, 199.

(45) Gabaldon, J. P.; Bore, M.; Datye, A. K. *Top. Catal.* **2007**, *44*, 253.

(46) Idakiev, V.; Tabakova, T.; Tenchev, K.; Yuan, Z. Y.; Ren, T. Z.; Su, B. L. *Catal. Today* **2007**, *128*, 223.

(47) Pietron, J. J.; Stroud, R. M.; Rolison, D. R. *Nano Letters* **2002**, *2*, 545.

(48) Carrettin, S.; Concepcion, P.; Corma, A.; Nieto, J. M. L.; Puntes, V. F. *Angew. Chem.-Int. Ed.* **2004**, *43*, 2538.

(49) Zhang, X.; Wang, H.; Xu, B. Q. *J. Phys. Chem. B* **2005**, *109*, 9678.

(50) Glaspell, G.; Hassan, H. M. A.; Elzatahry, A.; Fuoco, L.; Radwan, N. R. E.; El-Shall, M. S. *J. Phys. Chem. B* **2006**, *110*, 21387.

(51) Han, Y. F.; Zhong, Z. Y.; Ramesh, K.; Chen, F. X.; Chen, L. W. *J. Phys. Chem. C* **2007**, *111*, 3163.

(52) Zhong, Z.; Ho, J.; Teo, J.; Shen, S.; Gedanken, A. *Chem. Mater.* **2007**, *19*, 4776.

(53) Moreau, F.; Bond, G. C. *Appl. Catal., A* **2006**, *302*, 110.

(54) Corti, C. W.; Holliday, R. J.; Thompson, D. T. *Top. Catal.* **2007**, *44*, 331.

(55) Lai, S. Y.; Zhang, H. X.; Ng, C. F. *Catal. Lett.* **2004**, *92*, 107.

JP804250F